# Mass assembly history and infall time of the Fornax dwarf spheroidal galaxy

Mei-Yu Wang,[1]★ Louis E. Strigari,[1] Mark R. Lovell,[2,3] Carlos S. Frenk[4] and Andrew R. Zentner[5]

[1]*Department of Physics and Astronomy, Mitchell Institute for Fundamental Physics and Astronomy, Texas A&M University, College Station, TX 77843-4242, USA*
[2]*GRAPPA, Universiteit van Amsterdam, Science Park 904, NL-1098 XH Amsterdam, the Netherlands*
[3]*Instituut-Lorentz for Theoretical Physics, Niels Bohrweg 2, NL-2333 CA Leiden, the Netherlands*
[4]*Institute for Computational Cosmology, Durham University, South Road, Durham DH1 3LE, UK*
[5]*Department of Physics and Astronomy, and Pittsburgh Particle physics, Astrophysics, and Cosmology Center (Pitt PACC), University of Pittsburgh, Pittsburgh, PA 15260, USA*

## ABSTRACT

We use cosmological simulations to identify dark matter subhalo host candidates of the Fornax dwarf spheroidal galaxy using the stellar kinematic properties of Fornax. We consider cold dark matter (CDM), warm dark matter (WDM), and decaying dark matter (DDM) simulations for our models of structure formation. The subhalo candidates in CDM typically have smaller mass and higher concentrations at $z = 0$ than the corresponding candidates in WDM and DDM. We examine the formation histories of the ∼100 Fornax candidate subhaloes identified in CDM simulations and, using approximate luminosity–mass relationships for subhaloes, we find two of these subhaloes that are consistent with *both* the Fornax luminosity and kinematics. These two subhaloes have a peak mass over 10 times larger than their $z = 0$ mass. We suggest that in CDM the dark matter halo hosting Fornax must have been severely stripped of mass and that it had an infall time into the Milky Way of ∼9 Gyr ago. In WDM, we find that candidate subhaloes consistent with the properties of Fornax have a similar infall time and a similar degree of mass-loss, while in DDM we find a later infall time of ∼3–4 Gyr ago and significantly less mass-loss. We discuss these results in the context of the Fornax star formation history, and show that these predicted subhalo infall times can be linked to different star formation quenching mechanisms. This emphasizes the links between the properties of the dark matter and the mechanisms that drive galaxy evolution.

**Key words:** methods: numerical – Galaxy: evolution – Galaxy: kinematics and dynamics – dark matter.

## 1 INTRODUCTION

The temperature anisotropies in the cosmic microwave background (CMB) anisotropy spectrum measured by the *Wilkinson Microwave Anisotropy Probe* (*WMAP*; Hinshaw et al. 2013) and *Planck* (Planck Collaboration XVI 2014), and observations of the large-scale ($k \lesssim 0.1$ Mpc $h^{-1}$) galaxy clustering spectrum measured by the 2dF Galaxy Redshift Survey (Cole et al. 2005) and Sloan Digital Sky Survey (Tegmark et al. 2006) have shown that the large-scale structure formation is consistent with the $\Lambda$ cold dark matter (CDM) model (Frenk & White 2012). The observation of the CDM com-

ponent implies physics beyond the standard model, and many dark matter candidates exist within extensions to the standard model of particle physics that behave as CDM (Jungman, Kamionkowski & Griest 1996). Though CDM is theoretically well-motivated, there are both theoretical (e.g. Abazajian et al. 2012; Zurek 2014) and observational (Weinberg et al. 2013; Boyarsky et al. 2014, 2015; Bulbul et al. 2014) interests in considering alternatives. In fact, a broad exploration of particle dark matter candidates finds that many viable models behave differently than CDM, particularly on small scales, implying that observations of dark matter structure on small scales may provide a unique test of different particle dark matter candidates.

Aside from the Magellanic Clouds, the eight brightest satellite galaxies of the Milky Way are dwarf spheroidal (dSph) galaxies and

the internal kinematics of these dSphs offer one of the best prospects for understanding the properties of particle dark matter from small-scale astronomical observations (for a recent review see Walker 2013). Stellar kinematics unambiguously indicate that the dSphs are dark-matter-dominated (Walker et al. 2007), and their measured potentials have been used to determine whether their dark matter profiles are consistent with an NFW density profile long predicted by CDM (Navarro, Frenk & White 1996, 1997). However, in spite of the high-quality data sets, at present it is unclear whether the data indicate that the dark matter distributions in dSphs are in conflict with the NFW model (Walker & Peñarrubia 2011; Amorisco, Agnello & Evans 2013) or are consistent with it (Breddels & Helmi 2013; Jardel et al. 2013; Strigari, Frenk & White 2014).

Improvements in *N*-body simulations and in hydrodynamic simulations of Milky Way-like dark matter haloes and their corresponding populations of subhaloes now provide even more detailed predictions for the dark matter distributions of the dSphs. Detailed fitting of the stellar kinematics and photometry to subhaloes in CDM *N*-body simulations indicate that the dSphs reside in dark matter haloes with maximum circular velocity of approximately 20–25 km s$^{-1}$ (Strigari, Frenk & White 2010). More general fits to the dSph stellar kinematics in alternative dark matter model simulations such as warm dark matter (WDM; Lovell et al. 2014), decaying dark matter (DDM; Wang et al. 2014), and self-interacting dark matter (SIDM; Vogelsberger, Zavala & Loeb 2012) indicate that the maximum circular velocities are larger than in CDM (Boylan-Kolchin, Bullock & Kaplinghat 2011). Recent CDM hydrodynamic simulations find that these dark-matter-only simulations neglect the important effect of baryons, which modify the $z = 0$ maximum circular velocities of dSphs by about 15 per cent (Zolotov et al. 2012; Brooks et al. 2013; Brooks & Zolotov 2014; Sawala et al. 2014, 2016). Even though baryonic physics is thought to be important for dark matter distribution in haloes, it is still in debate about how to quantify the effects correctly.

Identifying subhaloes that are consistent with hosting dSphs in CDM as well in alternative dark matter scenarios can shed light on the cosmological evolution of those subhaloes and, perhaps, the galaxies that they contain. Such identifications may pave the way for the development of specific predictions of both CDM and alternative models that can serve as true tests of the models. Exploiting stellar kinematics for this purpose is complementary to and significantly more robust than using predictions for the luminosities of galaxies within subhaloes, because these predicted luminosities are extremely uncertain and rely on extrapolating phenomenological scaling relations outside of their established domain (Garrison-Kimmel et al. 2014). It is additionally complementary to methods that utilize measurements of the orbital motions of Milky Way satellites (Rocha, Peter & Bullock 2012; Kallivayalil et al. 2013; Sohn et al. 2013).

In this paper we identify dark matter subhalo host candidates of the Fornax dSph in CDM, WDM, and DDM *N*-body simulations by matching to the observed kinematics and photometry. The non-CDM based models that we study exhibit DM free-streaming effects that are not present in CDM. For WDM models, previous studies suggest that an equivalent thermal relic mass $\sim$ keV generates a truncation of the matter power spectrum on scales $\sim$a few Mpc (Bode, Ostriker & Turok 2001). This effect suppresses the formation of small structure below the WDM free-streaming scale, resulting in delayed formation of haloes. Lovell et al. (2014) use galactic zoom-in simulations to show that typical galactic subhaloes are less concentrated than their CDM counterparts because they form at later times. Sterile neutrinos are a canonical WDM candidate,

and the decays of sterile neutrinos provide a possible origin for the detection of an unexplained X-ray line observed at 3.55 keV in the Galactic Centre, M31, and galaxy clusters (Boyarsky et al. 2014, 2015; Bulbul et al. 2014). In DDM models, the DM free-streaming is delayed since the excess velocity imparted from the DM decay is introduced with a lifetime comparable or greater to Hubble time. This can avoid the tight limits placed by high-redshift phenomena like Lyman $\alpha$ forest (Wang et al. 2013) and can impact galactic substructure (Wang et al. 2014). In DDM, at high redshift the structure formation is similar to CDM until the age of the Universe is comparable to decay lifetime (Wang & Zentner 2012).

We focus on the stellar kinematics of Fornax because it has a high-quality kinematic data sample and the dark matter potentials of subhaloes in all of our simulations are well-resolved on the scale of the Fornax half-light radius. With the candidate host subhaloes of Fornax identified, we determine the dynamical properties of the host subhaloes, such as the present day mass, the peak mass, and the maximum circular velocity. With candidate host subhaloes identified in each simulation, we examine the assembly histories of the Fornax host candidates. To assign luminosity to our Fornax candidates we use a simple relationship between the stellar mass and peak halo mass, and from this we identify Fornax subhalo candidates in CDM, WDM, and DDM that are consistent with both its kinematics and luminosity. These Fornax candidates allow us to predict the infall times and degree of tidal stripping of these subhaloes, and we use these quantities to connect to models for the Fornax star formation history in each simulation.

The outline of the paper is as follows. In Section 2, we briefly describe the properties of simulations used in our analysis. In Section 3 we review our procedures for identifying Fornax subhalo candidates using its stellar kinematic data and photometry data. In Section 4 we present our results for the subhalo assembly histories, and discuss how these quantities can be used to determine the Fornax infall time, star formation history, and quenching mechanisms. Lastly we draw our conclusions in Section 5.

## 2 SIMULATIONS

In this section we briefly describe the cosmological simulations that we utilize. For more details we refer to the original simulation papers (CDM: Springel et al. 2008, WDM: Lovell et al. 2014, and DDM: Wang et al. 2014).

For the CDM model, we utilize the Aquarius simulations, which are six realizations (Aquarius A to F) of galactic zoom-in simulations (Springel et al. 2008). These simulations are generated using the GADGET code (Springel et al. 2008) and use cosmological parameters consistent with the one-year and five-year *WMAP* data: $H_0 = 73$ km s$^{-1}$ Mpc$^{-1}$, $\Omega_{\rm m} = 0.25$, $\Omega_\Lambda = 0.75$, $\sigma_8 = 0.9$, and $n_s = 1$. We adopt the level-2 resolution as our main sample (with Plummer gravitational softening length $\epsilon = 65.8$ pc and particle mass $m_p = 1.399 \times 10^4$ M$_\odot$–$6.447 \times 10^3$ M$_\odot$), and utilize the highest level-1 resolution for Aquarius A (with $\epsilon = 20.5$ pc and particle mass $m_p = 1.712 \times 10^3$ M$_\odot$) to perform resolution tests to understand the effects of the force softening scale on our analysis. The details of these tests are described in the Appendix A. The properties of the Aquarius simulations are shown in Table 1. We note that the mass of six galactic haloes spans a wide range within the conventionally possible Milky Way host halo mass values. This allows us to investigate Fornax candidate formation histories in diverse environments in the CDM case.

**Table 1.** Parameters of simulations. The mass of the galactic halo $M_{200b}$ is defined as the mass enclosed within the region of 200 times of the background density.

| Simulations | Particle mass $m_p$ (M$_\odot$) | Force Softening $\epsilon$ (pc) | $M_{200b}$ (M$_\odot$) | $r_{200b}$ (kpc) | Dark matter properties |
|---|---|---|---|---|---|
| Aq-A1 | $1.712 \times 10^3$ | 20.5 | $2.52 \times 10^{12}$ | 433.5 | CDM |
| Aq-A2 | $1.370 \times 10^4$ | 65.8 | $2.52 \times 10^{12}$ | 433.5 | CDM |
| Aq-B2 | $6.447 \times 10^3$ | 65.8 | $1.05 \times 10^{12}$ | 323.1 | CDM |
| Aq-C2 | $1.399 \times 10^4$ | 65.8 | $2.25 \times 10^{12}$ | 417.1 | CDM |
| Aq-D2 | $1.397 \times 10^4$ | 65.8 | $2.52 \times 10^{12}$ | 433.2 | CDM |
| Aq-E2 | $9.593 \times 10^3$ | 65.8 | $1.55 \times 10^{12}$ | 368.3 | CDM |
| Aq-F2 | $6.776 \times 10^3$ | 65.8 | $1.52 \times 10^{12}$ | 365.9 | CDM |
| Aq-A2 w7 | $1.545 \times 10^4$ | 68.2 | $2.53 \times 10^{12}$ | 432.1 | CDM |
| Aq-A2-$m_{1.6}$ | $1.545 \times 10^4$ | 68.2 | $2.49 \times 10^{12}$ | 429.9 | WDM ($m_{WDM} = 1.6$keV) |
| Aq-A2-$m_{2.3}$ | $1.545 \times 10^4$ | 68.2 | $2.52 \times 10^{12}$ | 431.4 | WDM ($m_{WDM} = 2.3$keV) |
| Z13-CDM | $2.40 \times 10^4$ | 72.0 | $1.31 \times 10^{12}$ | 335.2 | CDM |
| Z13-t10-v20 | $2.40 \times 10^4$ | 72.0 | $1.16 \times 10^{12}$ | 336.2 | DDM ($\Gamma^{-1} = 10$ Gyr, $V_k = 20.0$ km s$^{-1}$) |

For the WDM models, we use the simulations described in Lovell et al. (2014). To account for WDM physics, Lovell et al. (2014) re-simulate the Aquarius A halo using initial condition wave amplitudes that are rescaled with thermal relic WDM power spectra from Viel et al. (2005). We adopt their 'high resolution' suite that corresponds to level-2 in the original Aquarius notation with $m_p = 1.55 \times 10^4$ M$_\odot$ with $\epsilon = 68.1$ pc. This suite includes two WDM simulations with equivalent thermal relic masses of 2.3 keV and 1.6 keV, and their CDM counterpart simulations. The 2.3 keV thermal relic is a good approximation to the matter power spectrum of a 7 keV sterile neutrino that is resonantly produced in a lepton asymmetry $L_6 \sim 20$, which translates to a transfer function warmer than that inferred from the 3.55 keV line (Lovell 2015; Venumadhav et al. 2015). We take 1.6 keV model as a case that is ruled out by current Lyman $\alpha$ forest limits (e.g. Viel et al. 2013) and 2.3 keV as the model likely allowed by such limits for comparison. The cosmological parameters are derived from WMAP7: $H_0 = 70.4$ km s$^{-1}$ Mpc$^{-1}$, $\Omega_m = 0.272$, $\Omega_\Lambda = 0.728$, $\sigma_8 = 0.81$, and $n_s = 0.967$. Note that this is different than the original Aquarius simulations for which *WMAP*1 cosmology was implemented. Therefore we denote this CDM run as 'Aq-A2-w7' to set apart from the original Aquarius A2 run (Aq-A2). We describe the effects of the different cosmology on our results in Appendix B. The self-bound haloes in Aquarius simulations and WDM simulations were identified using the SUBFIND algorithm (Springel et al. 2001).

For our DDM model, we use the set of simulations that implement late-time DDM physics from Wang et al. (2014). In these DDM models, a dark matter particle of mass $M$ decays into a less massive daughter particle of mass $m = (1 - f)M$ with $f \ll 1$ and a significantly lighter, relativistic particle, with a lifetime $\Gamma^{-1}$, where $\Gamma$ is the decay rate. The stable daughter particle acquires a recoil kick velocity, $V_k$, the magnitude of which depends upon the mass splitting between the decaying particle and the daughter particle. The DDM simulations are generated using a modified version of GADGET-3 (Peter, Moody & Kamionkowski 2010). Here we consider the case with decay lifetime $\Gamma^{-1} = 10$ Gyr and kick velocity $V_k = 20$ km s$^{-1}$. This model has been shown to have interesting implications for dark matter small-scale structure (Wang et al. 2014) and is allowed by current Lyman $\alpha$ forest limits (Wang et al. 2013). The cosmology used is based on *WMAP*7 results with $H_0 = 71$ km s$^{-1}$ Mpc$^{-1}$, $\Omega_m = 0.266$, $\Omega_\Lambda = 0.734$, $\sigma_8 = 0.801$, and $n_s = 0.963$. We use AMIGA HALO FINDER (AHF; Knollmann & Knebe 2009) for halo finding and the merger tree is constructed using CONSISTENT TREES (Behroozi et al.

2013a). Although two halo finders are used in analysing different simulation sets, the halo or subhalo properties are expected to be recovered with high consistencies. An example that compares the halo and subhalo property prediction of several halo finders can be found in Knebe et al. (2011).

We define the virial mass ($M_{200b}$) of the galactic halo as the mass enclosed within the region of 200 times the background for all simulations, which corresponds to the $M_{50}$ in Springel et al. (2008). We adopt this definition for the same reason quoted in Springel et al. (2008), namely that it yields the largest radius among other conventional halo definition and hence the largest number of substructures. The subhalo mass ($M_{sub}$) is the mass that is gravitationally bound to the subhalo. Defining the subhalo mass requires an operational definition of its 'outer edge' when it is inside the host halo potentials. We refer the reader to the respective papers, for example, the original Aquarius project paper (Springel et al. 2008), for the detailed definitions.

## 3 FITTING SUBHALOES TO STELLAR KINEMATICS

In this section we discuss our method for fitting subhaloes in simulations to the stellar kinematic and photometric data of Fornax. For our theoretical analysis we use the spherical Jeans equation, and allow for a constant but non-zero anisotropic stellar velocity dispersion. We utilize this theory in order to efficiently identify a large sample of Fornax candidates. For comparison studies with similar motivations have been undertaken (Boylan-Kolchin et al. 2011; Garrison-Kimmel et al. 2014) that have used the mass estimator of Walker et al. (2009b) and Wolf et al. (2010) to estimate maximum circular velocities for the dSphs. As we show below our results are in good agreement with these previous results. Since we start at the level of the Jeans equation, we are able to identify preferred orbital structure of the stars given the underlying subhalo potentials.

We assume that the potential is spherically symmetric, dispersion-supported, and in dynamical equilibrium, so that we can derive the stellar line-of-sight velocity dispersion profile as a function of projected radius $R$ (Binney & Mamon 1982):

$$\sigma_{los}^2(R) = \frac{2}{I_*(R)} \int_R^\infty \left[ 1 - \beta(r) \frac{R^2}{r^2} \right] \frac{\rho_*(r)\sigma_r^2 r}{\sqrt{r^2 - R^2}} dr \qquad (1)$$

with

$$I_*(R) = 2 \int_R^\infty \frac{\rho_*(r)r}{\sqrt{r^2 - R^2}} dr. \tag{2}$$

Here $\rho_*(r)$ is the 3D stellar density profile and $I_*(R)$ is its 2D projection. The velocity anisotropy parameter is $\beta(r) \equiv 1 - \sigma_t^2(r)/\sigma_r^2(r)$, where $\sigma_r(r)$ is the radial velocity dispersion of stars and $\sigma_t(r)$ is the tangential velocity dispersion. These quantities satisfy the Jeans equation (Binney & Tremaine 2008):

$$r \frac{d(\rho_* \sigma_r^2)}{dr} + 2\beta(r)\rho_* \sigma_r^2 = -\rho_*(r) \frac{GM(< r)}{r}. \tag{3}$$

For the case of constant non-zero $\beta$, the solution of equation (3) has a simple form:

$$\rho_* \sigma_r^2(r) = \frac{1}{r^{2\beta}} \int_r^\infty \frac{\rho_*(r') GM(< r') r'^{2\beta}}{r'^2} dr'. \tag{4}$$

To model the 3D stellar density profile $\rho_*(r)$ as a function of radius we use this general form:

$$\rho_*(r) \propto \frac{1}{x^a (1 + x^b)^{(c-a)/b}}, \tag{5}$$

where $x = r/r_0$ and $a, b, c$ are free parameters that capture the stellar distribution slopes over different radii. A density profile of this form has been found to adequately describe the photometry of the classical dSphs (Strigari et al. 2010). Though the conversion of 3D to 2D profile is not a one-to-one relation, implying that different choice of parameters for the 3D profiles can provide similar 2D projected profiles, the present photometry data do give good constraints on the Fornax stellar distributions with profiles of the form equation (5). We fix the normalization of stellar mass by assuming mass-to-light ration $M_*/L = 1$ and adopt the Fornax $V$-band luminosity value of $L_v = 1.7 \times 10^7 M_\odot$ (McConnachie 2012).

With the above equations we utilize the following algorithm to model the Fornax line-of-sight velocity dispersion given the subhaloes in each of our simulations. We begin by finding subhaloes in our galactic zoom-in simulations using halo finders, and for each subhalo determine the dark matter distribution and thus the potential as a function of radius. Given the potential of each subhalo, the stellar distribution described by the parameters $a, b, c, r_0$, and velocity anisotropy by $\beta$, we solve the Jeans equation to determine the line-of-sight velocity dispersion. We then fit to the photometric and kinematic data by marginalizing over these parameters $a, b, c, r_0$, and $\beta$ via a Markov Chain Monte Carlo (MCMC) method to determine the best-fitting value for the model parameters.

For our fits to the Fornax stellar kinematics we define

$$\chi_\sigma^2 = \sum_{i=1}^{N_{bins}} \frac{[\hat{\sigma}_i - \sigma_{los}(R_i)]^2}{\epsilon_i^2}, \tag{6}$$

where $N_{bins}$ is the number of annuli, $R_i$ is the mean value of the projected radius of stars in the $i$th annulus, and $\sigma_{los}(R_i)$ is the derived velocity dispersion for a given subhalo in the $i$th annulus. The line-of-sight velocity dispersion from the binned data is $\hat{\sigma}_i$ and the corresponding error is $\epsilon_i$ in each annulus.

The kinematic data sets that we use consist of line-of-sight stellar velocities from the samples of Walker et al. (2009a). We consider only stars with > 90 per cent probability of membership, which gives us a sample of 2409 Fornax member stars. We bin the velocity data in circular annuli and derive the mean line-of-sight velocity in each annulus as function of $R_i$. We calculate the line-of-sight velocity dispersion $\hat{\sigma}$ and their error $\epsilon$ in each annulus following the method described in Strigari et al. (2010).

For our fits to the Fornax photometry we define

$$\chi_{IR}^2 = \sum_{i=1}^{N_{IR}} \frac{[\hat{I}_*(R_i) - I_*(R_i)]^2}{\epsilon_{IR,i}^2}, \tag{7}$$

where $N_{IR}$ is the number of radial bins, $R_i$ is the radius of the $i$th data point, and $\hat{I}_*(R_i)$ is the observed 2D stellar surface density in the $i$th radius bin and $\epsilon_{IR,i}^2$ is the Poisson uncertainty. We note that for the simplicity of the calculation we adopt this $\chi^2$ form for the photometry data. However, this logarithmic form of the likelihood function is an approximation instead of its true form since the uncertainties of a small sample follow a Poisson distribution rather than a normal distribution. For our photometric data we use the measurements from Coleman et al. (2005). Note that in our analysis we assume that Fornax contains a single population of stars.

For our MCMC, we adopt uniform priors over the following range: $0 \leq a \leq 2$, $0.5 \leq b \leq 5$, $4 \leq c \leq 8$, $0.5 \leq r_0 \leq 2$, $-1.0 \leq \beta \leq 1.0$. The MCMC calculation is performed using a modified version of the publicly available code COSMOMC (Lewis & Bridle 2002) as an MCMC engine with our own likelihood functions. We adopt a simple form of the likelihood function as the summation of the $\chi^2$ from both the stellar kinematic data and photometry over their degree of freedom: $\chi_{tot}^2/d.o.f. = \chi_\sigma^2/d.o.f. + \chi_{IR}^2/d.o.f.$, where $\chi_\sigma^2$ and $\chi_{IR}^2$ are calculated using equations (6) and (7) with degree of freedom (d.o.f.) equal to number of data bins minus the number of free parameters plus one. We have 15 radial bins in the velocity dispersion data and 19 radial bins in the photometry light profile data. We then select the subhaloes that satisfy the condition of $\chi_{tot}^2/d.o.f. \leq 3.0$ as good-fits to the Fornax kinematic and photometry data. We choose these criteria in order to obtain a conservatively large subhalo sample of candidates that can host Fornax.

## 4 RESULTS

We now present the results of our analysis. We begin by presenting the properties of the dark matter subhaloes in the different simulations that are candidate Fornax hosts using stellar kinematics alone. We then combine with a simple model for subhalo luminosities to identify subhaloes that match both the luminosity and kinematics of Fornax, and present results for the assembly history of these subhaloes.

### 4.1 Properties of Fornax candidate host subhaloes at $z = 0$

In this subsection we discuss the properties of Fornax candidate host subhaloes at $z = 0$. We begin by discussing the density profiles. for which we compare the central densities of the subhaloes from the different simulations. We then discuss the total subhalo masses and maximum circular velocities of the host subhalo candidates.

#### 4.1.1 Subhalo density profiles and correlations

We begin by examining the density profiles of the subhaloes that provide good fits to the photometry and line-of-sight velocity dispersion profiles. Fig. 1 shows the line-of-sight velocity dispersions for three different representative subhaloes, one from each of the CDM, WDM, and DDM simulation. For CDM, here we choose the subhalo that has the minimum value of $\chi_{tot}^2/d.o.f.$, while for DDM and WDM we choose the subhaloes that have $\chi_{tot}^2/d.o.f. < 3$ and have the shallowest central density profiles. For WDM (DDM), the
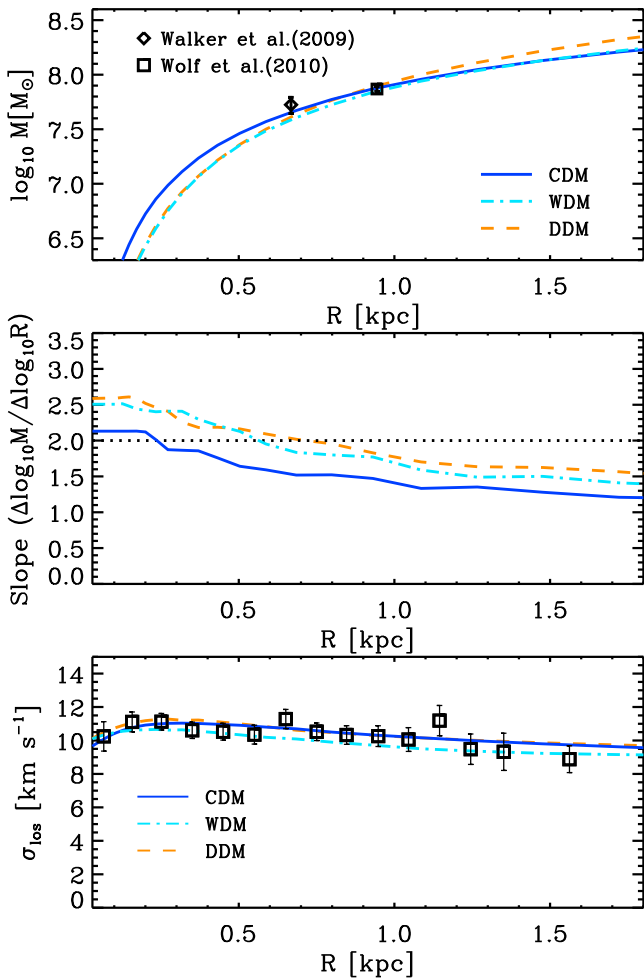
**Figure 1.** Top: DM distribution of subhaloes selected from three simulations with different DM models. The navy solid line represents a subhalo drawn from the Aquarius simulation (CDM), the aqua dash–dotted line is from the WDM simulation with WDM thermal relic mass = 2.3 keV, and the orange dash line is from the DDM simulations. These three subhaloes provide good-fits to the Fornax stellar kinematic profile and photometry data. Mass estimations for Fornax from previous studies are also shown. The squared data points with $1\sigma$ error bars show the mass estimation at the 3D half-light radius from Wolf et al. (2010), and the diamond points with $1\sigma$ error bars from Walker et al. (2009b). Middle: slopes of logarithmic mass profiles from these three subhaloes. The horizontal dash line marks where slope = 2, which is the theoretical predicted slope for NFW profiles as R → 0. The non-CDM subhaloes have slope > 2.0 in the inner region. Bottom: The best-fitting line-of-sight velocity dispersion derived using the Jeans equation formalism with $\beta$ = constant model.

$\chi^2_{\rm tot}$/d.o.f. is specifically 1.67 (0.85), and the p-value for the velocity dispersion fit is 0.4 (0.84). For the CDM subhalo, the $\chi^2_{\rm tot}$/d.o.f. is 0.93 while the p-value for the velocity dispersion fit is 0.8. Thus in all three cases the fits are good from a statistical standpoint.

Fig. 1 also shows both the mass distribution and the log-slopes as a function of radius of the selected subhaloes. The CDM subhalo is the most centrally concentrated at radii $\lesssim$ 500 pc, generating a central slope of $\Delta\log_{10}M/\Delta\log_{10}R \sim 2$, which is consistent with the predicted value from an NFW profile. The DDM subhalo has a central slope of ~2.6, while the WDM subhalo has a central slope of ~2.5. Thus the WDM subhaloes have 'soft' cores, which are expected since WDM subhaloes are less concentrated than their

CDM counterparts because they form at a later time (Lovell et al. 2012). The DDM subhalo has a slightly shallower core-like feature than in WDM because the effects of dark matter decay are scale-dependent (Wang et al. 2014).

As Fig. 1 indicates, the predicted line-of-sight velocity dispersions are very similar, even though the best-fitting values of $a$, $b$, $c$, $r_0$ and $\beta$ are different in each case. This highlights an explicit degeneracy between the dark matter potential, the velocity anisotropy, and the stellar density profile. At the level of a Jeans-based analysis, the degeneracy between the dark matter potential and the velocity anisotropy has been well-studied and has been known to preclude determination of the dark matter profile shape (Strigari, Bullock & Kaplinghat 2007).

The degeneracy between the stellar density profile and both the dark matter potential and the velocity anisotropy is less well-understood (see however Strigari et al. 2010, 2014), so it is interesting to examine this further within the context of a Jeans-based analysis. In Fig. 2 we examine the possible degeneracy for the case of a single subhalo by showing the correlation between the stellar density slope at $r = 600$ pc versus anisotropy parameter. For all models, within 68 per cent contour region $\beta$ spans a wide range and is degenerate with the stellar density concentration. The specific allowed regions change in each of the models, because they predict different DM density slopes. We observe modest degeneracy between stellar density slope and anisotropy parameter, and it is most significant in the DDM subhalo, for which the inner slope is the shallowest among the three subhaloes shown here. The weak degeneracies may be partially due to the fact that the current quality of the data is not enough to provide good constraints.

### 4.1.2 Subhalo masses and circular velocities

Though the density profiles of the CDM, WDM, and DDM subhaloes are indistinguishable when we apply Jeans equation formalism to fit the photometric and the kinematic data, the subhaloes are distinct when considering more global properties. In Fig. 3 we show the circular velocity curves, $V_{\rm circ} = \sqrt{GM(<r)/r}$, of subhaloes that provide good fits to the Fornax kinematic data and photometry data. Note that for each curve the stellar mass contribution has been included, so that at a radius of 0.9 kpc, the enclosed mass contribution from stars is about 10 per cent of the DM mass. The circular velocity curves in the WDM and DDM models are shallower in the centre than the CDM subhaloes, which is consistent with the discussion above on the individual best-fitting density profiles. Further, the WDM and DDM subhaloes have larger maximum value, $V_{\rm max}$, which is consistent with previous analyses (Lovell et al. 2012; Wang et al. 2014).

Fig. 4 shows the distribution of $V_{\rm max}$ and the total mass of the subhalo, $M_{\rm sub}$, for the CDM subhalo host candidates that are good fits to Fornax. Here we show only results from the CDM simulations Aq-A2-w7 and Z13, because from these simulations we are able to identify the subhalo counterparts from the WDM and DDM simulations, respectively. From Fig. 4 and also Table 2, we show that CDM host subhalo candidates have $10^8{\rm M}_\odot \leq M_{\rm sub} \leq 10^9{\rm M}_\odot$, $16\,{\rm km\,s^{-1}} \leq V_{\rm max} \leq 22\,{\rm km\,s^{-1}}$. Table 2 shows the average $M_{\rm sub}$ and $V_{\rm max}$ of Fornax candidates from all our simulations. As is indicated, Aq-A2-w7 and Z13 provide a good representation of our entire sample of CDM simulations. The $V_{\rm max}$ range of candidates from six Aquarius simulations (see Table 2) have an average ~17 km s$^{-1}$ and an associated small variance, which agree well with results from previous study (Boylan-Kolchin, Bullock & Kaplinghat 2012).
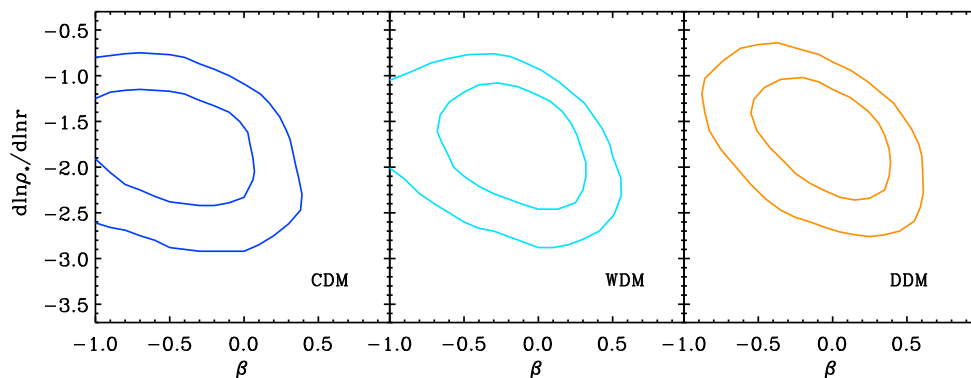
**Figure 2.** The 68 and 95 per cent contour region for the stellar density slope at r = 600 pc versus velocity anisotropy $\beta$. From left to right, the contours are drawn from the MCMC results of the Jeans equation fitting for the subhaloes shown in Fig. 1 (left: CDM, middle: WDM, right: DDM).
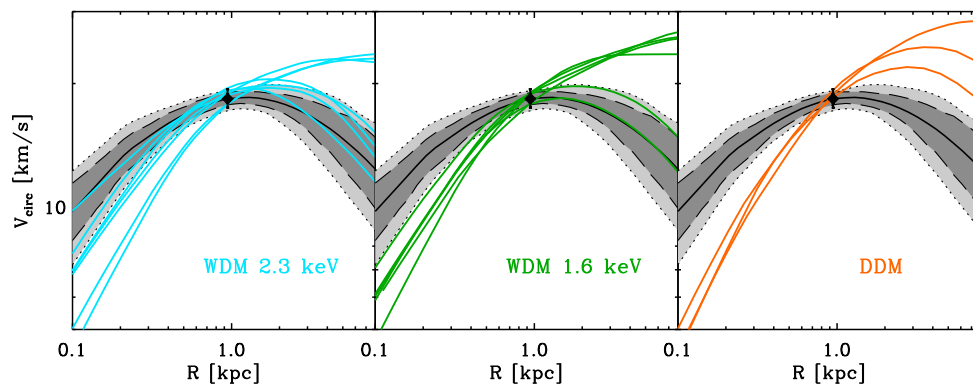


**Figure 3.** Circular velocity curves of subhaloes that are good fits to the Fornax stellar kinematic and photometry data. Notice that for each curve the stellar mass contribution has been included. The dark grey shaded areas include 68 per cent of the subhalo curves from Aquarius simulation A to F, and the light grey areas are for 95 per cent of the subhaloes. The solid black lines are the average of all the Aquarius CDM fits. From left to right-hand panel, the coloured lines show the subhaloes from the WDM simulation with 2.3 keV thermal relic mass (left-hand panel, aqua), the WDM simulation with 1.6 keV thermal relic mass (middle panel, green), and the DDM simulation with lifetime = 10 Gyr and kick velocity = 20 km s$^{-1}$ (right-hand panel, orange).

For comparison Fig. 4 shows the WDM and DDM subhaloes that match the Fornax kinematics and photometry. In the WDM simulation with 2.3 keV WDM mass we identify seven host subhalo candidates with $M_{sub} \sim 0.3$–$3 \times 10^9 M_{\odot}$ and $V_{max} \sim 18$–$23$ km s$^{-1}$. In the WDM simulation with 1.6 keV particle mass, we identify six host subhalo candidates with $M_{sub} \sim 0.2$–$8 \times 10^9 M_{\odot}$ and $V_{max} \sim 17$–$28$ km s$^{-1}$. In the DDM simulation we identify three host subhalo candidates with $M_{sub} \sim 0.8$–$4 \times 10^9 M_{\odot}$ and $V_{max} \sim 22$–$28$ km s$^{-1}$. These results indicate that from our Jeans-based modelling WDM and DDM predict a population of massive Fornax host subhaloes that have shallower central dark matter density profiles. We note that alternative DM scenarios always predict much fewer Fornax candidates than their CDM counterpart simulations, simply because the number of subhaloes are reduced significantly due to different DM properties. For example for the WDM case, fig. 11 in Lovell et al. (2014) shows that the numbers of subhaloes with $V_{max} \geq 15$ km s$^{-1}$ are 14 (1.6 keV), 28 (2.3 keV) and 120 (CDM). For the DDM case the subhalo number with $V_{max} \geq 15$ km s$^{-1}$ is 16 and 56 for the CDM counterpart. The subhalo numbers in different CDM haloes reflect mainly the differences in halo mass and merger history.

### 4.2 Predictions for luminosity and effects of reionization

To this point we have not used the luminosity of Fornax as a constraint, other than to consider its impact on the stellar kinematics and photometry. In doing so we have implicitly assumed that all of the subhaloes are suitable hosts of a galaxy with the present day luminosity of Fornax. We have made this assumption in order to analyse a large statistical sample of well-resolved Fornax host candidates in *N*-body simulations that do not account for the effects of baryons on the subhalo evolution. High-resolution Local Group simulations with baryons have been recently undertaken (Sawala et al. 2014, 2016), though at present the statistical sample of subhaloes is smaller in these simulations than the corresponding sample from *N*-body simulations. For this reason, we use semi-analytic models for the luminosities of our Fornax subhalo host candidates, and leave to a future study the analysis of the simulations that include the baryons.

Our subhalo luminosities are motivated by the results of several studies. First, we consider the results of Sawala et al. (2014), who utilize hydrodynamic simulations to predict the luminosity of subhaloes before they fall into the Milky Way halo and at $z = 0$. For subhaloes with the present day luminosity of Fornax, Sawala et al. find that subhaloes with the luminosity of Fornax have a total mass in the range $\sim 2$–$10 \times 10^9 M_{\odot}$, and a total peak halo mass in the range $\sim 7$–$20 \times 10^9 M_{\odot}$. The high end of this mass range is consistent with previous semi-analytic models (Cooper et al. 2010) and with the predictions from the abundance matching method (Behroozi, Wechsler & Conroy 2013b). For dSphs fainter than Fornax, the predicted range of subhalo masses for a fixed luminosity is larger, and also there are stronger deviations from the predictions of abundance matching and that of Sawala et al. (2014).
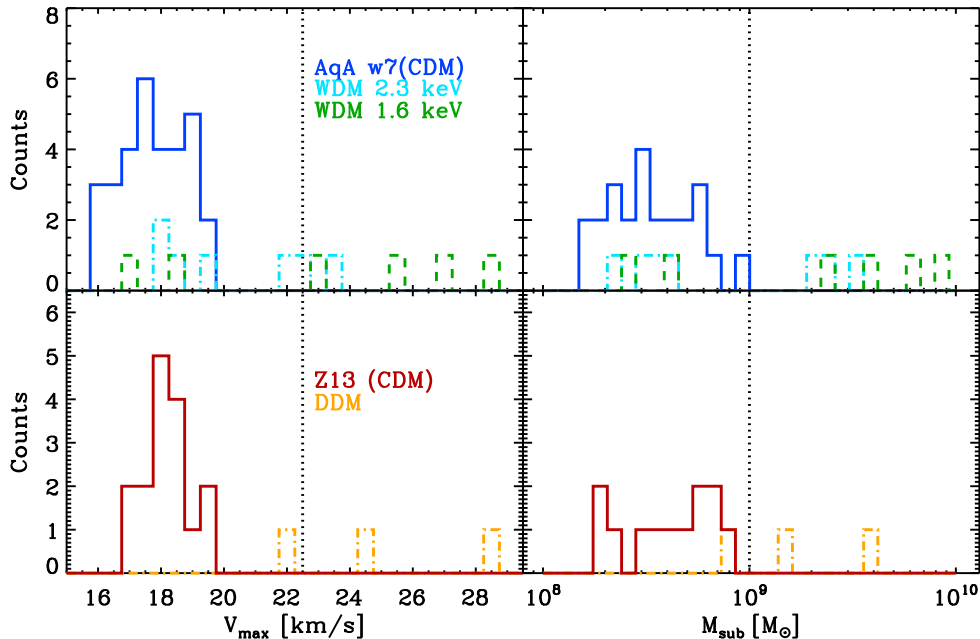
**Figure 4.** Histograms of subhalo properties for the Fornax good-fits. Here we show two subhalo present-time properties: maximum circular velocity ($V_{max}$, left-hand panels), and subhalo mass ($M_{sub}$, right-hand panels). In the upper two panels the navy histograms with solid lines show the Aquarius A results, the aqua ones with dash–dotted lines are for the WDM 2.3 keV simulation, and the green ones with dash lines are for the WDM 1.6 keV simulation. In the lower two panels the dark red histograms with solid lines show the Z13 CDM results, and the orange ones with dash–dotted lines are for the DDM simulation. We note that for the same galactic halo realization, the alternative DM scenarios presented here (WDM, DDM) generate much less substrucure than their CDM couterparts (see text in Section 4.1.2).

**Table 2.** Average subhalo properties of Fornax kinematic good-fits.

| Simulations | $M_{sub}$ (M$_\odot$) | $M_{peak}$ (M$_\odot$) | $V_{max}$ (km s$^{-1}$) |
|---|---|---|---|
| Aq-A2-w7 | $3.72 \pm 1.91 \times 10^8$ | $1.55 \pm 2.01 \times 10^9$ | $17.70 \pm 1.02$ |
| Aq-A2-$m_{2.3}$ | $1.30 \pm 1.32 \times 10^9$ | $4.23 \pm 2.09 \times 10^9$ | $20.31 \pm 2.26$ |
| Aq-A2-$m_{1.6}$ | $3.52 \pm 3.15 \times 10^9$ | $5.05 \pm 2.67 \times 10^9$ | $23.22 \pm 4.57$ |
| Z13-CDM | $4.50 \pm 2.00 \times 10^8$ | $8.77 \pm 2.94 \times 10^8$ | $18.26 \pm 0.71$ |
| Z13-t10-v20 | $2.11 \pm 1.78 \times 10^9$ | $4.87 \pm 5.10 \times 10^9$ | $25.03 \pm 3.18$ |
| Aq-A2 | $3.46 \pm 1.27 \times 10^8$ | $1.60 \pm 2.14 \times 10^9$ | $17.69 \pm 0.80$ |
| Aq-B2 | $2.34 \pm 1.06 \times 10^8$ | $1.04 \pm 1.76 \times 10^9$ | $17.78 \pm 0.98$ |
| Aq-C2 | $2.60 \pm 1.10 \times 10^8$ | $0.91 \pm 1.25 \times 10^9$ | $17.61 \pm 0.44$ |
| Aq-D2 | $3.40 \pm 2.30 \times 10^8$ | $8.28 \pm 4.23 \times 10^8$ | $17.81 \pm 1.13$ |
| Aq-E2 | $2.84 \pm 1.23 \times 10^8$ | $6.62 \pm 3.79 \times 10^8$ | $17.60 \pm 0.97$ |
| Aq-F2 | $3.58 \pm 2.43 \times 10^8$ | $1.00 \pm 0.59 \times 10^9$ | $17.98 \pm 1.04$ |
| Aq Average | $3.07 \pm 1.77 \times 10^8$ | $1.02 \pm 1.29 \times 10^9$ | $17.76 \pm 0.94$ |
| Aq Max | $1.18 \times 10^9$ | $8.83 \times 10^9$ | $21.71$ |
| Aq Min | $1.09 \times 10^8$ | $3.08 \times 10^8$ | $15.79$ |

A well-known caveat, however, is that the abundance matching technique is not calibrated at both sub-galactic scales and in non-CDM cosmologies. Therefore, results in these regimes depend on extrapolating the existing models and assuming the average galaxy formation history holds for non-CDM based models.

In order to determine the relevant peak subhalo mass range for Fornax, we first take the lower bound on the stellar mass of Fornax to be $M_* \gtrsim 1 \times 10^7$ M$_\odot$. The lower bound is derived from the $1\sigma$ lower bound on the Fornax $V$-band luminosity of $L_V = 1.7 \,^{+0.5}_{-0.4} \times 10^7$ L$_\odot$, and assuming a stellar mass-to-light ratio $M_*/L = 0.8$ ($M_* \sim 1.3 \times 10^7 \times 0.8$ M$_\odot$ for the lower bound). For this adopted stellar mass, we then select Fornax candidates by their peak mass that predict the same stellar mass range using the abundance matching description

in Behroozi et al. (2013b). In Fig. 5 we show the distribution of peak subhalo masses for these Fornax candidates. These results indicate that while subhaloes that are consistent with the Fornax kinematics have subhalo peak masses in the range $M_{sub} \sim 10^8$–$10^{10}$ M$_\odot$, only a handful at the very massive end predict the right luminosity. For example from the right-hand panel in Fig. 5 we find that 2 out of 124 candidates from the six Aquarius simulations are consistent with the Fornax luminosity. Interestingly, these two candidates come from the Aquarius A and B simulations, which are, respectively, the most massive and the least massive haloes among all six Aquarius simulations. This would indicate that the likelihood of generating a Fornax candidate may be only weakly correlated with the galactic halo mass.

For comparison, in Fig. 5 we show the Fornax candidates from the WDM and DDM simulations, as well as their CDM counterparts. Though the sample of host subhaloes is smaller than in the case of CDM, there is a higher probability for WDM and DDM Fornax candidates to reside in more massive subhaloes. Therefore, the WDM and DDM candidates are more likely to match the bright luminosity of Fornax than the CDM candidates. In each case, we find 1–2 candidates that match the kinematics and luminosity, out of 3–7 candidates that just match the kinematics. Note again the caveat that the relationship between the stellar mass and subhalo progenitor mass may differ from this relation which is derived from CDM simulations.

With candidate host subhaloes identified we are now in position to study their evolution and the masses of their progenitors near the redshift of reionization. The effect of reionization on suppressing star formation in small haloes shows that haloes below a few $10^8$ M$_\odot$ likely have no stars due to the UV-background suppression. This implies that any subhalo with a progenitor less massive would be unlikely to host a visible galaxy today (Okamoto et al. 2008; Sawala et al. 2014).
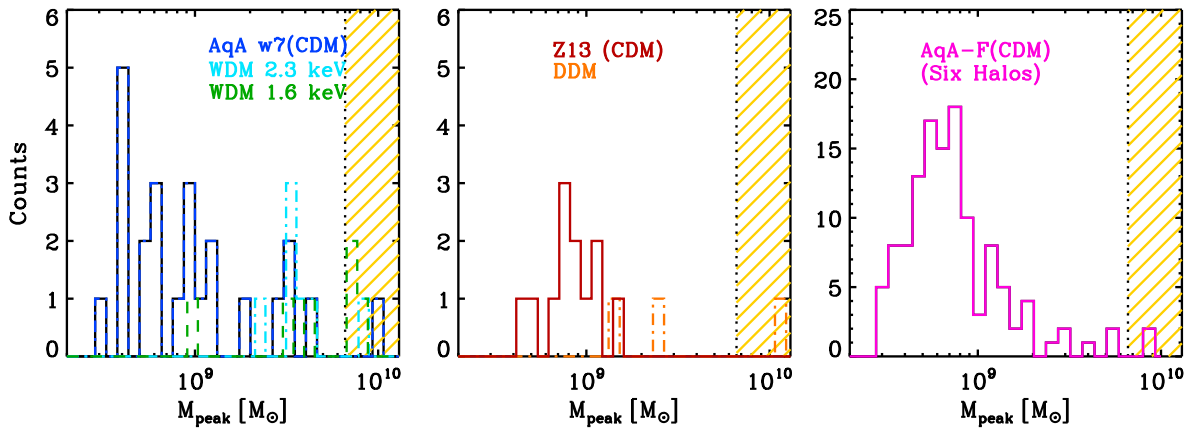
**Figure 5.** The $M_{peak}$ distribution of the Fornax good-fit subhaloes. The colour and line style notation in the left-hand panel is the same as previous figures, and the right-hand panel shows the distribution from all six Aquarius level-2 simulations (A–F). We note that there is only one galactic halo realization in the left and middle panel, while there are six in the left-hand panel. The yellow shaded areas indicate the region where the luminosity of these objects are consistent with the Fornax luminosity using abundance matching methods from Behroozi et al. (2013b).
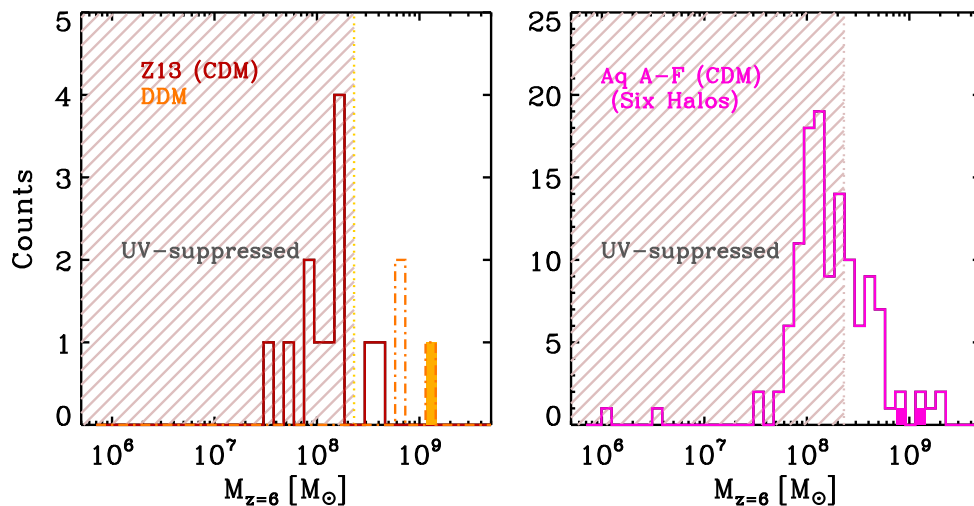


**Figure 6.** The distribution of the progenitor mass at $z = 6$ for the Fornax candidates. The colour and line style scheme in the left-hand panel is the same as Fig. 4 showing DDM and Z13 simulation candidates, and right-hand panel shows all the candidates from all six Aquarius haloes. We note that there is only one galactic halo realization in the left-hand panel, while there are six in the left-hand panel. The filled histograms indicate the subhaloes with luminosity that match Fornax at $z = 0$. The shaded areas indicate the progenitor mass range with baryon content subject to UV background suppression (Okamoto et al. 2008).

In Fig. 6 we show the subhalo progenitor mass at $z = 6$ for the Fornax candidates. According to the criteria of Okamoto, Gao & Theuns (2008), more than half of the Fornax candidate in Aquarius would not host any stars. The subhaloes that match both the Fornax kinematic and photometry data as well as the luminosity are on the massive end of the distribution.

In the left-hand panel of Fig. 6 we show the case for the DDM simulation and its CDM counterpart. We do not include WDM simulations here because their structure formation and galaxy formation at high redshift are expected to be significantly different than in CDM. Also for the WDM models that we considered here, majority of the subhalo progenitors are not yet formed or identified by halo finders at $z = 6$. However, for the DDM model with a decay lifetime of 10 Gyr, it is safe to assume a similar reionization history as CDM. Since at $z = 6$ less than about 10 per cent of the dark matter has decayed with a small recoil kick velocity of $20 \, \mathrm{km \, s^{-1}}$, the structure growth of both the dark matter and baryon components should be similar to CDM. Again the majority of the CDM

subhaloes should be UV-suppressed, and all three DDM subhaloes are above the threshold, with one object that matches the Fornax luminosity.

### 4.3 Mass assembly histories

We now move on to discuss the mass assembly histories of our Fornax candidates. The left-hand panel of Fig. 7 shows the subhalo mass as a function of redshift for all 124 of our Fornax candidates from all six Aquarius haloes. The middle panel shows the corresponding candidates from the WDM model with 2.3 keV mass and the right-hand panel shows the candidates from DDM simulations. From the discussion above, we identify the subhaloes that match the Fornax luminosity, and also determine an approximate infall time for those subhaloes that match both the Fornax luminosity and kinematics. From Aquarius simulations, we can see that the candidates that match the kinematics and luminosity, which are shown in blue lines rather than the grey lines for candidates only fit stellar
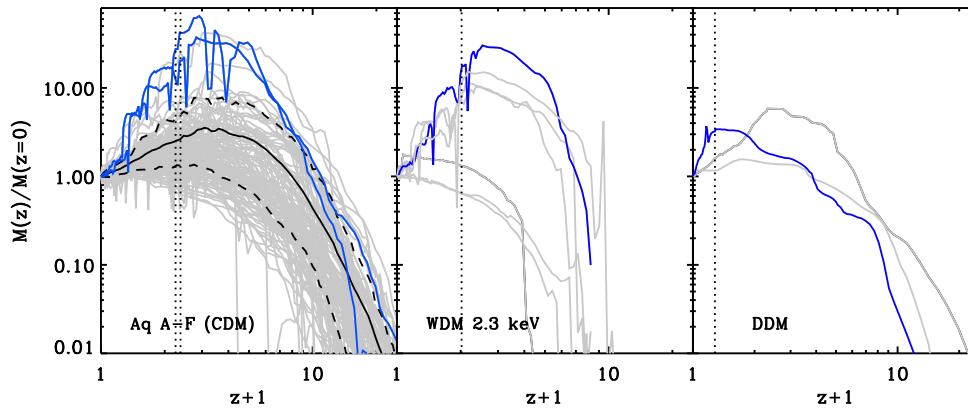
**Figure 7.** Mass assembly histories for the Fornax good-fit subhaloes. The light grey lines show the fits with luminosity dimmer than Fornax using abundance matching technique from Behroozi et al. (2013b), and the dark blue lines show those with luminosity that matches the Fornax luminosity. The vertical dotted lines show the infall time of the blue curves. In the left-hand panel the dashed black lines include 68 per cent of the Aquarius simulation fits, and the black solid lines show the mean value.

kinematics, also have the largest ratio of $M(z_{peak})/M(z = 0)$, with typical peak values for this ratio of $\sim$30–60 at $z \sim$2. For WDM, subhaloes that match the kinematics and luminosity also show a large peak value at $z \sim 1.5$. On the other hand the corresponding DDM subhalo shows a relatively low peak value of $M(z_{peak})/M(z = 0) \sim 3$ at $z \lesssim 1$.

From the results presented in Fig. 7, we can identify three important trends and predictions regarding tidal stripping, infall times, and star formation histories.

### 4.3.1 Tidal stripping

Using the above results in CDM we have a clear prediction that Fornax has lost a significant amount of dark matter mass after it falls into the Milky Way. Does this translate into a more specific observational signature? One possibility is that this tidal stripping of dark matter is manifest in the tidal stripping of the stars. However, since our models only directly include dark matter, it is not clear whether we should expect stellar tidal tails to be observable. It is possible that the stellar components are embedded deeply in the centre of the subhalo potential, so that the dark matter is mostly stripped and the stars left unstripped. For example, Watson, Berlind & Zentner (2012) shows that if subhaloes experience substantial dark matter mass-loss before mass is lost within the galaxy, this explains how satellite galaxies lose stellar mass and contribute to 'intrahalo light' (IHL).

For comparison the Fornax candidates in WDM, shown in the middle panel of Fig. 7, are similar to CDM in that both require large $M_{peak}/M(z = 0)$. In DDM, as shown in the right-hand panel of Fig. 7, the ratio is much smaller, $M_{peak}/M(z = 0) \sim 3$. These results hint at the interesting possibility that hosts of Fornax have undergone different degrees of tidal stripping in different dark matter models. Thus with future larger statistical samples of non-CDM models, as well as the inclusion of baryons in the simulation, the degree of tidal stripping of Milky Way-satellites may provide a new test of dark matter models.

### 4.3.2 Infall time

From the peaks in the evolution of the subhalo masses in Fig. 7, we can identify the infall times of the subhaloes into the Milky Way halo. In CDM, the subhaloes that match the Fornax kinematics

and luminosity have infall redshifts of $z = 1.25$ and $z = 1.37$, corresponding to lookback times of $\sim$9 Gyr. For the 2.3 keV WDM model the infall redshift is $z = 1.02$, corresponding to a lookback time of $\sim$8 Gyr. For DDM model the infall redshift is at $z = 0.28$, corresponding to a lookback time of $\sim$3 Gyr. So the DDM host subhalo is predicted to fall into the Milky Way more recently than the CDM and WDM candidates.

It is informative to compare the lookback times that we deduce to previous estimates of the infall times of Milky Way satellites. Rocha et al. (2012) estimate infall times using subhalo Galactocentric positions and orbital motions from Via Lactea II simulation. Using these criteria Fornax is most likely to have fallen into the Milky Way halo $\sim$5–9 Gyr ago. So even though our criteria for identifying Fornax subhalo candidates in CDM simulations are different from those in Rocha et al. (2012), the infall times are in good agreement. We note that the Aquarius simulations that we utilize and our stricter matching criteria using luminosity and stellar kinematic data allows for a larger range of merger histories than considered in Rocha et al. (2012), who utilize a single Milky Way halo.

### 4.3.3 Star formation quenching mechanism

The quenching of star formation in Milky Way dSphs may be related to their infall times. For example ram-pressure stripping can remove the cold gas at the centre of the satellites as a result of the high-speed interaction with the hot gas halo of the host halo (Gunn & Gott 1972). Ram pressure stripping has been invoked as the quenching mechanism for Milky Way and M31 dwarf satellites with $M_\star \lesssim 10^8 \, M_\odot$ with an extremely short quenching time-scale $\sim$2 Gyr (Fillingham et al. 2015).

As shown in Fig. 8, Fornax is observed to have an enhanced star formation activity $\sim$3–4 Gyr ago and quenching $\sim$2 Gyr ago (Coleman & de Jong 2008). If we match these time-scales with the infall times that we determined above, the enhanced star formation event is most consistent with the infall time of our DDM subhalo candidate. The grey shaded area shows the possible Fornax infall time range from Rocha et al. (2012). This covers a large infall time range including those predicted by the CDM and WDM simulations. However, it is interesting to note that other recent Fornax star formation history studies either indicate similar peak at $\sim$4 Gyr (de Boer et al. 2012) or draw different conclusions with a star formation peak at $\sim$8 Gyr (del Pino et al. 2013). Deep photometric studies of
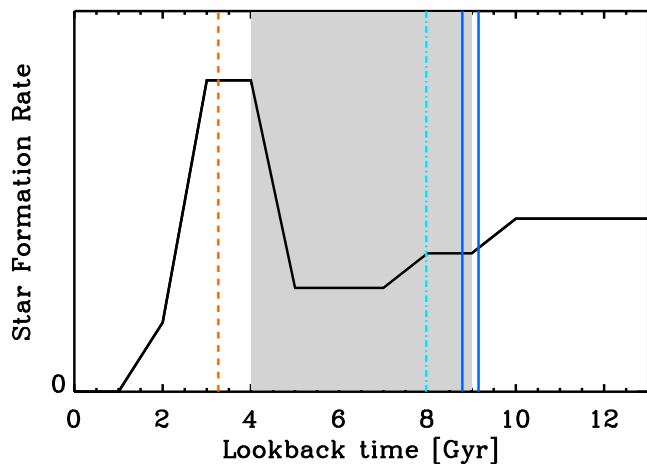
**Figure 8.** Qualitative Fornax star formation histories (black solid lines, from Coleman & de Jong 2008) compared to estimated infall times from Rocha et al. (2012) using Galactocentric positions and orbital motions (grey filled area) and our results (vertical dashed lines). The two solid navy dashed lines indicate the infall time for the two CDM candidates from the Aquarius simulations that match both the Fornax luminosity and stellar kinematics. The aqua dash–dotted line is for the WDM 2.3 keV candidate, and the orange dash line is for the DDM candidate. Notice the DDM candidate infall time is significantly lower than the Rocha et al. (2012) prediction and our CDM and WDM candidates, and also it happens at the time when the Fornax star formation rate starts to drop after a burst 3–4 Gyr ago. All others predict infall times before the enhanced star formation event.

Fornax will help resolve this discrepancy and provide more insight on the connection of the Fornax star formation history with its infall time.

To explain the Fornax star formation history in the context of the earlier subhalo infall times predicted in our CDM and WDM models, we can consider a scenario in which the Fornax star formation was quenched when it merged into Milky Way halo ∼9 Gyr ago. A close encounter with the Milky Way at the last perigalactic passage would then trigger star formation. This mechanism has been invoked to explain the star formation history of Leo I (Mateo, Olszewski & Walker 2008), which had a burst in its star formation ∼3–4 Gyr ago. Indeed proper motion and line-of-sight velocity measurements indicate that Leo I is likely on a fairly eccentric, nearly unbound orbit (Sohn et al. 2013). In contrast with Leo I, Fornax likely has a much less eccentric orbit (Lux, Read & Lake 2010; Piatek et al. 2007), so a much closer encounter with the Milky Way may be more difficult to invoke in the case of Fornax. More precise measurement of orbital velocity and detailed orbit reconstruction will shed more light on this issue.

## 5 CONCLUSIONS AND DISCUSSION

We have fit the kinematics and photometry of the Fornax dSph to subhalo potentials predicted by numerical simulations of different dark matter models. CDM subhalo candidates are typically in the mass range of $10^8$–$10^9$ M$_\odot$. WDM and DDM models predict on average larger mass subhalo hosts of Fornax.

The diversities of subhalo candidate properties in different dark matter models and the different time evolution of dark matter free-streaming effects lead to diversities in subhalo formation history, and also likely their stellar formation history. With this in mind we utilize simulation merger trees to investigate the formation history of the subhaloes that match the Fornax kinematics. We implement

simple models to match the Fornax luminosity to dark matter halo mass in order to understand possible star formation histories of these Fornax subhalo candidates. Under the assumption that the mass of the most massive progenitor is correlated with the current stellar content in each galaxy, we derive current stellar masses for each subhalo.

For CDM subhaloes, our best candidates require the ratio between the peak mass and current mass to be $\gtrsim 10$. This suggests that these systems experience significant tidal stripping after they fall into Galactic halo and are subject to substantial dark matter mass-loss. It also implies that their infall times are $\gtrsim 9$ Gyr ago, so that they fall well inside the galactic halo where the tidal stripping is efficient. Interestingly, similar findings also have been pointed out by Cooper et al. (2010) using Aquarius simulations with a 'particle tagging' technique to simulate Galactic stellar haloes. Using Fornax and Carina as two examples, these authors find that they can only match their observed dwarf galaxy surface brightness and velocity dispersion profiles simultaneously by choosing model satellites that have suffered substantial tidal stripping.

Our WDM subhalo candidates show only mild deviation from their CDM counterparts, in that they have similar peak mass to current mass ratio and infall time. A caveat to this analysis is the real stellar content might be different, and full hydrodynamic simulations are needed to calibrate galaxy formation process in WDM. For the DDM candidates, using similar assumptions our subhalo candidates have relatively small peak mass/current mass ratio (∼3) and they are more massive at $z = 0$ than the CDM candidates. Therefore, the DDM candidate only experiences mild mass-loss since merging into the Galactic halo approximately 3 Gyr ago.

We note that our results are not yet able predict the existence of visible stellar tidal tails. Since galaxies are embedded deep in the centre of the halo potential, most of the tidal stripping effects are expected to be on the DM component. Determining whether or not stars are stripped out requires *N*-body simulations with star particles. Cooper et al. (2010) have shown that 20 per cent of the stellar mass and 2 per cent of DM mass of their Fornax candidate remains at present time. Also recent work from Battaglia, Sollima & Nipoti (2015) have examined the tidal effects on Fornax along its possible orbits. Current and forthcoming wide-field deep imaging surveys may be sensitive to faint stellar tidal tails and can provide an observational test of our models. Bate et al. (2015) use data from VLT Survey Telescope (VST) ATLAS Survey to study a region of 25 deg$^2$ centred on Fornax. They have excluded a shell structure outside of Fornax's tidal radius that was reported from a previous study (Coleman et al. 2005). In the near future the Dark Energy Survey (DES) will cover a wide area around Fornax with much improved imaging depth, and possibly provide a test of the tidal stripping hypothesis.

We find that most of the subhalo candidates are subject to the cosmic reionization UV-background so that their star formation is highly suppressed. In our sample more than half of the CDM candidates are likely not visible at all due to reionization. For the WDM model the reionization history is more uncertain because high-redshift structure formation is significantly delayed. However, for DDM the early structure formation follows CDM until late times when the decay process becomes significant, so a similar reionization history can be applied. Most of our DDM candidates are not affected by the UV-background since they are already massive at $z = 6$. This is largely because for the same Fornax kinematic data, DDM candidates tend to be more massive because they have less concentrated DM profiles than their CDM counterparts.

The difference in Fornax infall times in the different models may imply a different star formation quenching mechanism if environmental effects play an important role in dSph formation processes. From the observed Fornax star formation history, there is an enhanced star formation event at 3–4 Gyr ago and it is quenched ∼2 Gyr ago (Coleman & de Jong 2008). For those subhalo candidates that have infall times well before the star formation peak, star formation may be triggered by a close passage to the Milky Way. For those that have infall times after the star formation peak, the infall into Galactic halo may cause rapid gas loss due to ram-pressure stripping. More precise predictions can be made by detailed Fornax orbital motion reconstruction from its proper motion and line-of-sight velocity measurement, which may be possible with the *GAIA* satellite. Larger sets of simulations that sample more possible halo formation histories in different dark matter scenarios will also help to confirm our results.

## ACKNOWLEDGEMENTS

## REFERENCES

Abazajian K. et al., 2012, preprint (arXiv:1204.5379 )
Amorisco N. C., Agnello A., Evans N. W., 2013, MNRAS, 429, L89
Bate N. F., McMonigal B., Lewis G. F., Irwin M. J., Gonzalez-Solares E., Shanks T., Metcalfe N., 2015, MNRAS, 453, 690
Battaglia G., Sollima A., Nipoti C., 2015, MNRAS, 454, 2401
Behroozi P. S., Wechsler R. H., Wu H.-Y., Busha M. T., Klypin A. A., Primack J. R., 2013a, ApJ, 763, 18
Behroozi P. S., Wechsler R. H., Conroy C., 2013b, ApJ, 770, 57
Binney J., Mamon G. A., 1982, MNRAS, 200, 361
Binney J., Tremaine S., 2008, Princeton Univ. Press, Princeton, NJ
Bode P., Ostriker J. P., Turok N., 2001, ApJ, 556, 93
Boyarsky A., Ruchayskiy O., Iakubovskyi D., Franse J., 2014, Phys. Rev. Lett., 113, 251301
Boyarsky A., Franse J., Iakubovskyi D., Ruchayskiy O., 2015, Phys. Rev. Lett., 115, 161301
Boylan-Kolchin M., Bullock J. S., Kaplinghat M., 2011, MNRAS, 415, L40
Boylan-Kolchin M., Bullock J. S., Kaplinghat M., 2012, MNRAS, 422, 1203
Breddels M. A., Helmi A., 2013, A&A, 558, A35
Brooks A. M., Zolotov A., 2014, ApJ, 786, 87
Brooks A. M., Kuhlen M., Zolotov A., Hooper D., 2013, ApJ, 765, 22
Bulbul E., Markevitch M., Foster A., Smith R. K., Loewenstein M., Randall S. W., 2014, ApJ, 789, 13
Cole S. et al., 2005, MNRAS, 362, 505

Coleman M. G., de Jong J. T. A., 2008, ApJ, 685, 933
Coleman M. G., Da Costa G. S., Bland-Hawthorn J., Freeman K. C., 2005, AJ, 129, 1443
Cooper A. et al., 2010, MNRAS, 406, 744
de Boer T. J. L. et al., 2012, A&A, 544, A73
del Pino A., Hidalgo S. L., Aparicio A., Gallart C., Carrera R., Monelli M., Buonanno R., Marconi G., 2013, MNRAS, 433, 1505
Fillingham S. P., Cooper M. C., Wheeler C., Garrison-Kimmel S., Boylan-Kolchin M., Bullock J. S., 2015, MNRAS, 454, 2039
Frenk C., White S. D., 2012, Ann. Phys., 524, 507
Garrison-Kimmel S., Boylan-Kolchin M., Bullock J. S., Kirby E. N., 2014, MNRAS, 444, 222
Gunn J. E., Gott J. R., III, 1972, ApJ, 176, 1
Hinshaw G. et al., 2013, ApJS, 208, 19
Jardel J. R., Gebhardt K., Fabricius M. H., Drory N., Williams M. J., 2013, ApJ, 763, 91
Jungman G., Kamionkowski M., Griest K., 1996, Phys. Rep., 267, 195
Kallivayalil N., van der Marel R. P., Besla G., Anderson J., Alcock C., 2013, ApJ, 764, 161
Knebe A. et al., 2011, MNRAS, 415, 2293
Knollmann S. R., Knebe A., 2009, ApJS, 182, 608
Lewis A., Bridle S., 2002, Phys. Rev. D, 66, 103511
Lovell M. R. et al., 2012, MNRAS, 420, 2318
Lovell M. R., Frenk C. S., Eke V. R., Jenkins A., Gao L., Theuns T., 2014, MNRAS, 439, 300
Lovell M. R. et al., 2015, preprint (arXiv:1511.04078)
Lux H., Read J. I., Lake G., 2010, MNRAS, 406, 2312
McConnachie A. W., 2012, AJ, 144, 4
Mateo M., Olszewski E. W., Walker M. G., 2008, ApJ, 675, 201
Navarro J. F., Frenk C. S., White S. D. M., 1996, ApJ, 462, 563
Navarro J. F., Frenk C. S., White S. D. M., 1997, ApJ, 490, 493
Okamoto T., Gao L., Theuns T., 2008, MNRAS, 390, 920
Peter A. H. G., Moody C. E., Kamionkowski M., 2010, Phys. Rev. D, 81, 103501
Piatek S., Pryor C., Bristow P., Olszewski E. W., Harris H. C., Mateo M., Minniti D., Tinney C. G., 2007, AJ, 133, 818
Planck Collaboration XVI, 2014, A&A, 571, A16
Polisensky E., Ricotti M., 2014, MNRAS, 437, 2922
Rocha M., Peter A. H. G., Bullock J., 2012, MNRAS, 425, 231
Sawala T. et al., 2014, preprint (arXiv:1412.2748)
Sawala T. et al., 2016, MNRAS, 456, 85
Sohn S. T., Besla G., van der Marel R. P., Boylan-Kolchin M., Majewski S. R., Bullock J. S., 2013, ApJ, 768, 139
Springel V., White S. D. M., Tormen G., Kauffmann G., 2001, MNRAS, 328, 726
Springel V. et al., 2008, MNRAS, 391, 1685
Strigari L. E., Bullock J. S., Kaplinghat M., 2007, ApJ, 657, L1
Strigari L. E., Frenk C. S., White S. D. M., 2010, MNRAS, 408, 2364
Strigari L. E., Frenk C. S., White S. D. M., 2014, preprint (arXiv:1406.6079)
Tegmark M. et al., 2006, Phys. Rev. D, 74, 123507
Venumadhav T., Cyr-Racine F.-Y., Abazajian K. N., Hirata C. M., 2015, preprint (arXiv:1507.06655)
Viel M., Lesgourgues J., Haehnelt M. G., Matarrese S., Riotto A., 2005, Phys. Rev. D, 71, 063534
Viel M., Becker G. D., Bolton J. S., Haehnelt M. G., 2013, Phys. Rev. D, 88, 043502
Vogelsberger M., Zavala J., Loeb A., 2012, MNRAS, 423, 3740
Walker M., 2013, in Oswalt T. D., Gilmore G., eds, Planets, Stars and Stellar Systems, Vol. 5. Springer Science+Business Media Dordrecht, p. 1039
Walker M. G., Peñarrubia J., 2011, ApJ, 742, 20
Walker M. G., Mateo M., Olszewski E. W., Gnedin O. Y., Wang X., Sen B., Woodroofe M., 2007, ApJ, 667, L53
Walker M. G., Mateo M., Olszewski E. W., Sen B., Woodroofe M., 2009a, AJ, 137, 3109
Walker M. G., Mateo M., Olszewski E. W., Peñarrubia J., Wyn Evans N., Gilmore G., 2009b, ApJ, 704, 1274
Wang M.-Y., Zentner A. R., 2012, Phys. Rev. D, 85, 043514

Wang M.-Y., Croft R. A. C., Peter A. H. G., Zentner A. R., Purcell C. W., 2013, Phys. Rev. D, 88, 123515

Wang M.-Y., Peter A. H. G., Strigari L. E., Zentner A. R., Arant B., Garrison-Kimmel S., Rocha M., 2014, MNRAS, 445, 614

Watson D. F., Berlind A. A., Zentner A. R., 2012, ApJ, 754, 90

Weinberg D. H., Bullock J. S., Governato F., Kuzio de Naray R., Peter A. H. G., 2013, preprint (arXiv:1306.0913)

Wolf J., Martinez G. D., Bullock J. S., Kaplinghat M., Geha M., Muñoz R. R., Simon J. D., Avedo F. F., 2010, MNRAS, 406, 1220

Zentner A. R., Bullock J. S., 2003, ApJ, 598, 49

Zolotov A. et al., 2012, ApJ, 761, 71

Zurek K. M., 2014, Phys. Rep., 537, 91

# APPENDIX A: RESOLUTION TESTS AND CORRECTIONS

As pointed out in Boylan-Kolchin et al. (2012) where they used Aquarius simulations to compare dynamic properties of simulated galactic subhaloes with observed Milky Way satellites, the effect of force softening will introduce errors to the subhalo potentials in the central region. The reason is that the force softening scales of our simulations range from $\epsilon = 65.8$–$72.0$ pc. The effect of force softening will reduce the density on scales of $\sim 3\,\epsilon$. However, we need to work with a cumulative mass profile that will carry the effect to larger scale. In order to estimate and further correct for this effect, here we utilize the Aquarius A level 1 simulation, which has the same halo realization as the Aquarius A level 2 simulation but with much smaller force softening length ($\epsilon = 20$ pc) and particle mass ($m_p = 1.712 \times 10^3$ M$_\odot$), to test different correction methods to reconstruct the mass distribution at subhalo centre.

The correction method adopted here is similar to the one in Boylan-Kolchin et al. (2012). We have tried out a few different fitting ranges and correction ranges to find the one that gives the best results. The procedure is as follows. We fit the subhalo density

profiles with an Einasto profile, which has the following form:

$$\rho(r) = \rho_{-2} \exp\left(-\frac{2}{\alpha}\left[\left(\frac{r}{r_{-2}}\right)^\alpha - 1\right]\right). \tag{A1}$$

The fitting range is $[r_{\mathrm{inner}}, r_{\mathrm{upper}}]$, where $r_{\mathrm{upper}}$ is the smaller of 3 kpc or 1.5 $r_{\mathrm{max}}$ and we try a few different values for $r_{\mathrm{inner}}$. We then replace the mass within $r_{\mathrm{inner}}$ with the accumulated mass generated from the Einasto profile fit:

$$M(<r) = \frac{4\pi r_{-2}^3\,\rho_{-2}}{\alpha}\exp\left(\frac{3\ln\alpha + 2 - \ln 8}{\alpha}\right)\gamma\left[\frac{3}{\alpha}, \frac{2}{\alpha}\left(\frac{r}{r_{-2}}\right)^\alpha\right] \tag{A2}$$

and use the mass profile from simulations outside of the $r_{\mathrm{inner}}$.

In Fig. A1 we compare the Fornax data fitting results using different corrections with different $r_{\mathrm{inner}}$ on Aquarius level 2 subhaloes to their Aquarius level 1 counterparts. Here we show three different $r_{\mathrm{inner}}$ choices: no correction ($r_{\mathrm{inner}} = \infty$, red histograms in Fig. A1), $r_{\mathrm{inner}} = 300$ pc [close to choice of 291 pc in Boylan-Kolchin et al. (2012), blue histograms in Fig. A1], and 200 pc (green histograms in Fig. A1). We take the ratio of the fitting parameter value from Aquarius level 2 subhaloes with their level 1 counterparts. So the ideal case will be they lie very close to 1, indicating that the corrections faithfully recover the mass distribution in higher resolution simulation runs.

We can see that some of the parameters are not affected much by the correction. Examples are $c$ and $r_0$, since they are related to stellar distribution in the outer region (for example, $r_0 \sim 1$ kpc) and are not sensitive to the correction in the inner region ($\lesssim 300$ pc). The $\chi^2$ of the photometry data fit also is not affected significantly, since most of the photometry data points are distributed outside $\lesssim 300$ pc. The worst of all parameters is $a$, and the amount of deviation seems to be large no matter which correction we apply.
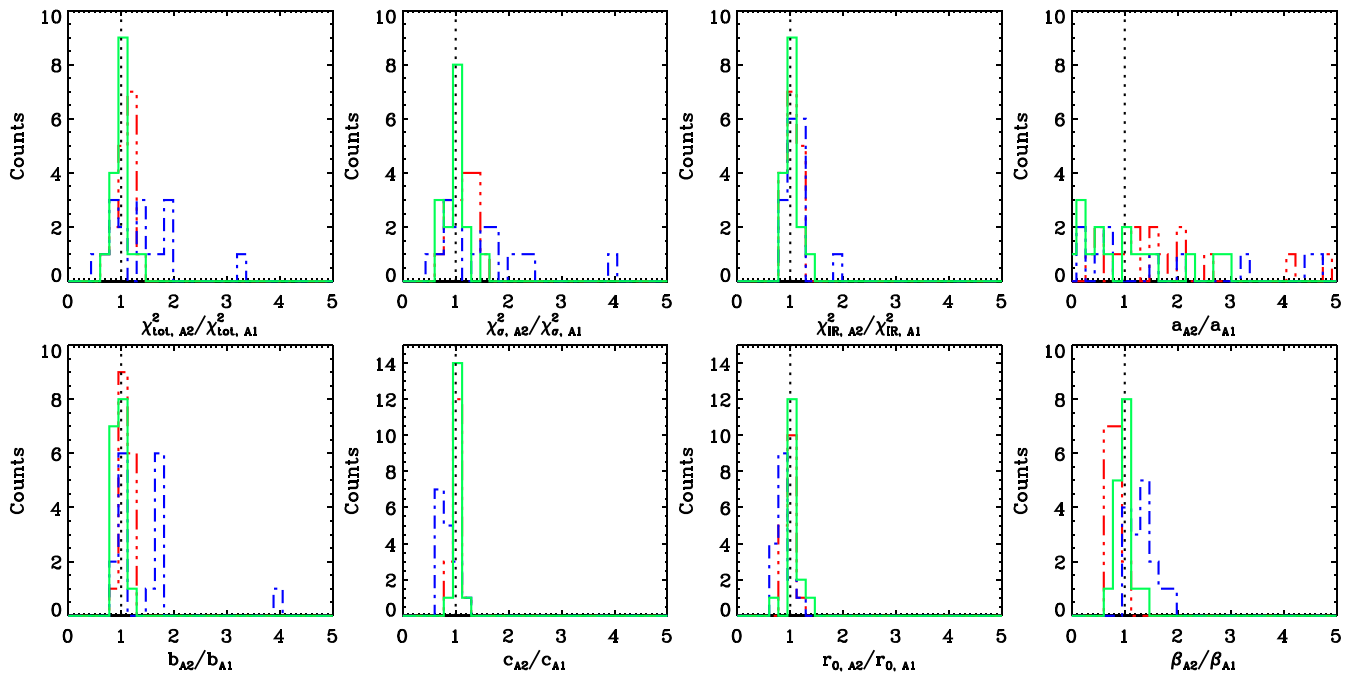


**Figure A1.** The distribution of the fitting results for Aquarius A-2 simulations with different softening scale correction methods: no correction (red histograms with dash–triple-dotted lines); blue histograms with dash–dotted lines are for $r_{\mathrm{inner}} = 300$ pc; green histograms with solid lines are for $r_{\mathrm{inner}} = 200$ pc. Here $r_{\mathrm{inner}}$ is within what radius a Einasto profile fit is used for accumulated mass profile. The $x$-axes show the ratio of fits to their Aquarius level 1 counterparts.
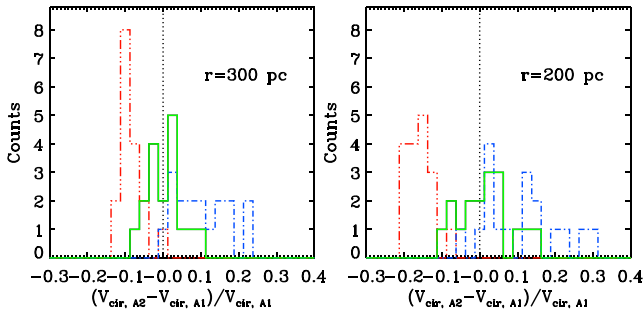
**Figure A2.** The distribution of circular velocity ($V_{cir}$) fractional difference for different Aquarius A resolution simulations and different softening scale correction methods. The *x*-axis shows the fractional difference of the $V_{cir}$. The colour and line style scheme is the same as Fig. A1.

The reason is that the data do not provide good constraints on the parameter *a*. The uncertainty of the MCMC result for *a* is usually very large and highly correlated with other parameters such as the parameter that determines the normalization of the photometry data. So the wide distribution of the parameter *a* for different corrections is likely not due to the way the dark matter potential is corrected, but due to the large uncertainties from the poor constraints and parameter correlations. From the overall behaviour of these three different correction methods, we can see that the green histograms, for which the Einasto profile correction is applied within 200 pc, show the best agreement with Aquarius level 1 counterparts.

In Fig. A2 we show the fractional difference in circular velocity between Aquarius level 1 subhaloes and their level 2 counterparts after corrections at two radii: r = 200 and 300 pc. At 300 pc the difference is within 20 per cent and at 200 pc the difference is within 30 per cent for all correction methods. However, before applying any correction, the difference is negative (red histograms) and for the correction applied within 300 pc (blue histograms) the difference is biased towards positive values. The green histogram, which is for the correction within 200 pc, is peaked at zero and with difference within 10–15 per cent. This indicates that before any corrections the central dark matter potentials ($V_{cir} = \sqrt{GM(r<)/r}$) are reduced due to softening scale effects for Aquarius level 2 simulations, and the suppression is up to about 20 per cent. However, if we apply the correction method suggested in Boylan-Kolchin et al. (2012), we can 'overcorrect' the potentials up to 20–30 per cent at 200–300 pc.
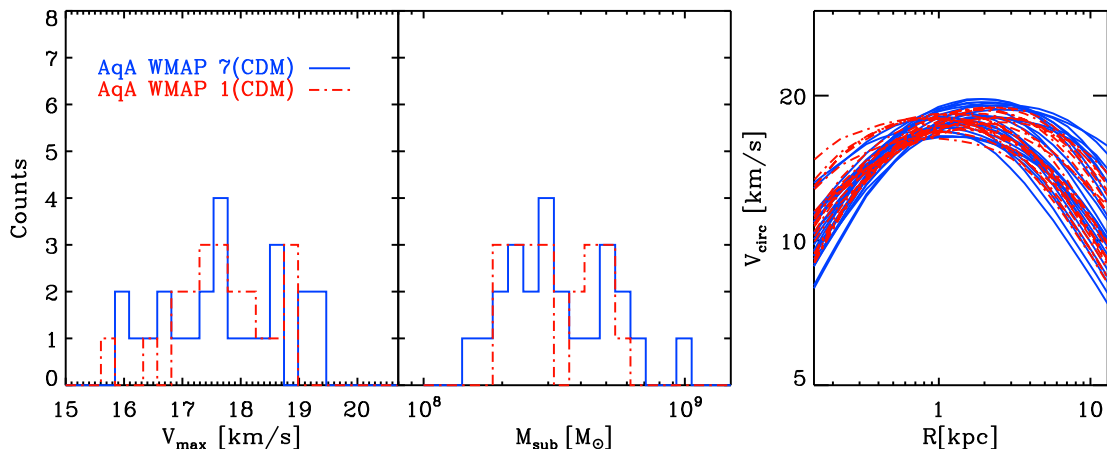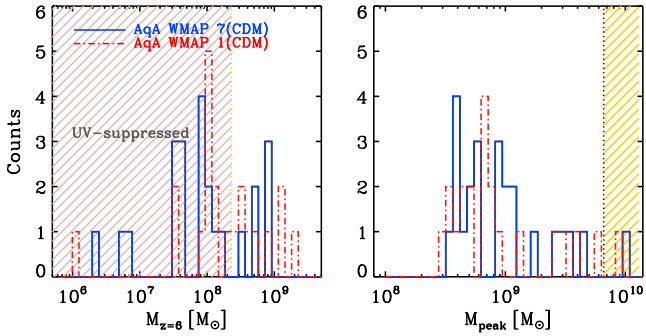
Therefore our tests show that a mild correction within 200 pc with the fitted Einasto profile mass will generate the best results for removing the softening scale effects. We thus adopt the correction all the simulations in this study.

## APPENDIX B: EFFECTS OF *WMAP*1 AND *WMAP*7 COSMOLOGICAL PARAMETERS

Here, we test the effects of different cosmological parameters on our study. Previous studies (e.g. Zentner & Bullock 2003; Polisensky & Ricotti 2014) have shown that different cosmological parameter values, especially $\sigma_8$ and $n_s$, have non-negligible effect to the substructure density profiles. The simulation sets used in our study have adopted different cosmological parameter values. We compare the Fornax Jeans equation fitting results from the Aquarius A Level-2 simulation that is re-simulated with a *WMAP*7 cosmology (Aq-A2-w7) with those from the original Aquarius A Level-2 simulation that is simulated with a *WMAP*7 cosmology (Aq-A2). One of the most significant differences of their choice of parameters lies in the difference in $\sigma_8$ ($\sigma_8 = 0.9$ for Aq-A2 while $\sigma_8 = 0.81$ for Aq-A2-w7). In the following, we will compare the fitting results and discuss the impacts due to the differences in cosmological parameters.

In Fig. B1 we show the present-time subhalo properties of the Fornax candidates and their circular velocity curves. Those are candidates that fit Fornax kinematics but not necessarily fit the Fornax luminosity. In both simulations we find a comparable number of good-fits. Here we only show those we can find counterparts in both simulations. Their maximum circular velocities ($V_{max}$) and subhalo mass ($M_{sub}$) span very similar range. However, it is shown in the right-hand panel in Fig. B1 that those subhalos from Aq-A2 are slightly more concentrated at the centre than those from Aq-A2-w7. As discussed in Polisensky & Ricotti (2014), haloes in simulations with higher $\sigma_8$ form earlier and thus are more concentrated. However, we can see from the distribution of candidate subhalo properties that the changes due to the differences in *WMAP*1 and *WMAP*7 cosmology are much smaller than the difference due to different dark matter properties. When we compare Fig. B1 with Fig. 4, we can see that WDM and DDM simulations generate subhaloes that exhibit very different properties that occupy a completely different subhalo property region. It is thus clear that high-quality Fornax data have provided good constraints on subhalo present-time properties.



**Figure B1.** Subhalo properties at $z = 0$: maximum circular velocity ($V_{max}$, left-hand panel), and subhalo mass ($M_{sub}$, middle panel), and circular velocity profiles (right-hand panel) for the Fornax good-fits from AqA *WMAP*1 (red dash–dotted lines) & AqA *WMAP*7 (blue solid lines) simulations. Here, we only show those we can find counterparts in both simulations.

We also investigate the differences in halo formation history. In Fig. B2 we check the distribution of $M_{peak}$ and mass at $z = 6$ of Fornax candidates from these two simulations. We find that the difference is mild and does not affect our conclusion. For example, for both simulations more than half of the candidates may have suppressed star formation due to the UV-background from reionization. Also for both simulations only one candidate matches the Fornax luminosity while others are much dimmer. Thus we conclude that the difference in *WMAP*1 and *WMAP*7 is mild and it has limited effects on both present-time properties and halo formation history. The differences due to dark matter properties, which is the focus of our study, exhibit much stronger effects.

**Figure B2.** The $M_{peak}$ and mass at $z = 6$ ($M_{z=6}$) distribution of the Fornax good-fits from the AqA *WMAP*1 (blue solid histogram) and AqA *WMAP*7 (red dash–dotted histogram) simulations. The shaded area in the left-hand panel indicates the progenitor mass range with baryon content that is subject to the UV background suppression. The yellow shaded area in the right-hand panel indicates the region where the luminosity of these objects are consistent with the Fornax luminosity using abundance matching methods from Behroozi et al. (2013b).

This paper has been typeset from a TEX/LATEX file prepared by the author.